Vorticity-Based Flow Structures and Cavitation Evolution in High-Pressure Submerged Waterjet

S. Teng[1], H. X. Liu[2†], C. Kang[1] and W. B. Zhang[3]

[1] School of Energy and Power Engineering, Jiangsu University, Zhenjiang, Jiangsu, 212013, China
[2] School of Materials Science and Engineering, Jiangsu University, Zhenjiang, Jiangsu, 212013, China
[3] Shanghai Marine Equipment Research Institute, Shanghai, 200031, China

†Corresponding Author Email: liuhx@mail.ujs.edu.cn

Abstract

The present study aims to describe flow structures and cavitation phenomenon in the submerged waterjet. A non-intrusive experimental work was performed. The waterjet was produced through a nozzle characterized by a short straight segment adjacent to the nozzle outlet. Waterjet pressures were varied from 5 to 22 MPa. The time-resolved particle image velocimetry (TR-PIV) was used to measure velocity distributions. The proper orthogonal decomposition (POD) method was employed to extract flow structures from the flow-measurement results. Cavitation was created through increasing the waterjet pressure. A comparison of cavitation patterns at different waterjet pressures was implemented. Similarity of the distribution of average velocity is revealed as the waterjet pressure varies. The POD results indicate that two high-vorticity bands close to the nozzle, symmetrically distributed with respect to the nozzle axis, dominate the waterjet stream. Further downstream, small-scale flow structures are sparsely distributed and assume a low percentage of the total energy. Initial cavitation is featured by small-scale cavities which are formed near the high-vorticity zone. As the waterjet pressure increases, the volume fraction of cavitation increases and morphological features of cavitation change significantly as waterjet develops. At a later stage, stable cavity clouds are evidenced. A high relevance between vorticity distribution and cavitation cloud pattern is demonstrated.

Nomenclature

A_{ij}	covariance matrix	t	time
D	outlet diameter of nozzle	TR-PIV	Time-Resolved Particle Image Velocimetry
f_{cav}	cavitation evolution frequency	V	two-dimensional matrix
L_{cav}	attainable streamwise distance of cavitation cloud	v_{mn}	elements in the matrix
m_i	number of velocity fields	α^i	eigenvalues
p	waterjet pressure	$\{\alpha^i\}$	eigenvector
POD	Proper Orthogonal Decomposition	α_j^i	the jth element of the eigenvector

1. INTRODUCTION

The submerged waterjet is characterized by drastic interaction between a waterjet stream and ambient water. The kinetic energy of the submerged waterjet attenuates rapidly due to the resistance from ambient water. Meanwhile, intensified mixing occurs at the waterjet stream edge, causing entrainment of ambient water into the waterjet stream. At high waterjet pressures, cavitation, a distinct phase-change phenomenon, may occur. The utilization of waterjet cavitation has been evidenced in applications such as surface hardening and industrial cleaning (Soyama and Takeo 2016). Since the nozzle associated with high jet pressures generally has small size, the waterjet stream immediately downstream of the nozzle is highly coherent. It is such a waterjet stream segment that contains concentrated energy and is responsible for high aggressivity of the waterjet.

The difficulty in studying high-pressure waterjet originates largely from the small temporal and spatial scales involved. The tools used to identify these scales are required to be highly sensitive. The nozzles with small outlet diameters are associated with thin waterjet streams. The flow phenomena related to these waterjet streams have never been overemphasized (Petkovšek and Dular 2013). Moreover, high waterjet pressure causes high velocity gradients at the edge of the waterjet stream, which provide a stimulus for the formation of cavitation (Gopalan *et al.* 1999). It proves that cavitation in the submerged waterjet is influenced by multiple factors such as nozzle geometry, liquid property and waterjet pressure (Soyama 2017). In most occasions, these factors are not independent; therefore, it is not an easy task to differentiate the effect of any individual factor from the others. This serves as a pertinent answer to why most conclusions about the waterjet cavitation obtained so far cannot be generalized.

Non-invasive flow measurement and visualization techniques have lent their significant support to the understanding of the submerged waterjet (Peng *et al.* 2018). Flow structures such as the vortices arising at the edge of the waterjet stream can be depicted based on the results of flow measurement. Moreover, the loss of jet stability can be judged from the flow patterns acquired. The application of the high-speed photography (HSP) technique enables the recording of transient flow phenomena. Furthermore, with the assistance of the micro-lens, the HSP technique allows a clear imaging of the phenomena with small temporal and spatial scales in the thin waterjet stream (Wilms *et al.* 2014). Apart from the HSP technique, the particle image velocimetry (PIV) technique can be used to visualize flow patterns in the submerged waterjet. At high waterjet velocities, the advantages of the time-resolved PIV (TR-PIV) technique are apparent due to the high image-acquisition frequencies that can be attained. Hitherto, the exercise of using TR-PIV for waterjet measurement has been devoted to the cases with low waterjet velocities (Cheng *et al.* 2011). In comparison, investigating high-pressure submerged waterjet using TR-PIV has rarely been reported.

Waterjet cavitation is closely related to the waterjet flow itself. However, the evolution of waterjet cavitation is characterized by intermittency, which is incompatible with variations of average waterjet parameters (Nobel and Talmon 2012). Furthermore, simultaneous measurement of waterjet velocity and cavitation morphology is difficult to accomplish using available experimental techniques. Literally, several experimental methods have been attempted in the study of waterjet cavitation. Even the specimen impacted by a cavitating waterjet could be used as a sensor. Then the residual stress, hardened layer and cavitation erosion patterns of such a sensor were measured and hence used to describe the characteristics of waterjet cavitation (Hu *et al.* 2010). From another aspect, acoustic and vibration signals could be used to evaluate the energy released by the collapse of cavitation bubbles (Kang *et al.* 2018).

The purpose of the present study is to describe the relationship between flow structures and cavitation phenomenon for the high-pressure submerged waterjet. Waterjet pressures were varied from 5 to 22 MPa. A nozzle with a short straight segment upstream of the nozzle outlet was selected. The time-resolved particle image velocimetry was used to measure waterjet velocity. The proper orthogonal decomposition (POD) method was used to extract dominant flow structures and to quantify the energy distribution among different POD modes. Cavitation was induced through increasing the waterjet pressure. Cavitation inception and cavitation development were monitored and described. Morphological features of cavitation at different stages of cavitation evolution were compared. The relationship of waterjet flow characteristics and cavitation was established.

2. EXPERIMENTAL SET-UP

2.1 Submerged Waterjet System

A schematic view of the experimental rig is shown in Fig.1. High waterjet pressures are provided by a plunger pump. The maximum waterjet pressure is 23.5 MPa. The nozzle is fixed on a supporting frame and the vertical and the horizontal positions of the nozzle can be adjusted. The water tank is measured 1800 mm in length and 500 mm in width. Therefore, waterjet can fully develop in both streamwise and transverse directions. The tank wall is made of plexiglass and the wall thickness is 20 mm, enabling non-invasive measurement and visualization of the waterjet flow. A weir plate is mounted at the downstream end of the tank. During the experiment, the liquid level in the tank was maintained constant, and the influence of free surface oscillation was therefore negligible (Shimada *et al.* 2004). The tank is sufficiently spacious and the time span for each experiment case is shorter than 10 minutes; therefore, the temperature rise of water in the tank could be neglected.
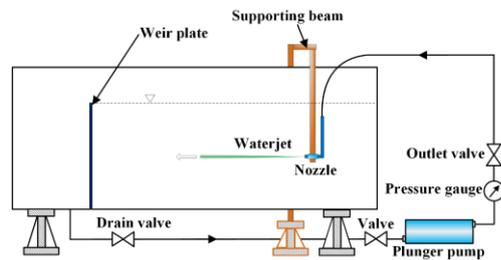

Fig. 1. Submerged waterjet experiment rig

The cross section of the nozzle is schematically shown in Fig.2. The nozzle outlet diameter D is 3.0 mm, and the length of the straight flow passage upstream of the nozzle outlet is 3.0 mm as well. With such a nozzle, a sudden expansion of the

waterjet stream as the waterjet is discharged from the nozzle is perceivable. In addition, this nozzle differs remarkably from that specified in the ASTM G134 standard (2010). For the standardized nozzle, the flow passage contains an expansion segment upstream of the nozzle outlet; therefore, the coherent part of the waterjet stream can sustain for a long downstream distance. For the nozzle considered here, as waterjet leaves the nozzle, the waterjet stream expands rapidly and then mixes with ambient water intensively. In practice, diverse nozzle geometries have been attempted due to a wide application of the nozzle in many engineering processes. The near-nozzle segment of the water jet stream depends largely on geometry of the flow passage in the nozzle, which has been demonstrated (Macian *et al*. 2003). The outlet diameter of the high-pressure nozzle is generally small; therefore, a subtle change of local geometry of the flow passage, such as the variation of the length of the straight segment upstream of the nozzle outlet, may trigger a considerable variation of the waterjet flow pattern. Furthermore, it was argued that waterjet cavitation is greatly related to the flow inside the nozzle passage (Giorgi *et al*. 2013). At the high waterjet pressures adopted here, it is impractical to visualize flows inside a transparent nozzle. A comparison of the cavitation erosion capability between different nozzles verified a significant effect of the shape of the flow passage inside the nozzle on waterjet cavitation (Soyama 2013).

During the experiment, the waterjet discharged from the nozzle mainly develops in horizontal direction. As indicated in Fig. 2, the streamwise direction is parallel with positive x direction of the rectangular coordinate system; meanwhile, the origin of the coordinate system is positioned at the center of the nozzle outlet section.
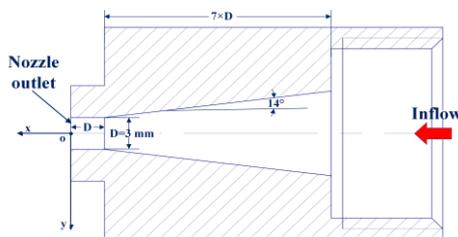

Fig. 2. Cross-sectional view of the nozzle

2.2 Optical Configuration

A LaVision TR-PIV system was used to measure waterjet velocity near the nozzle. Such a system is mainly composed of a Photonics DM30-527DH high-intensity laser generator, a Photron FASTCAM UX200 camera with frequencies ranging from 1 kHz to 10 kHz, a water-cooling system and the data-processing code DaVis. The configuration of major optical components is presented in Fig. 3(a). Light is emitted from the bottom, avoiding the influence of the wavy free surface, as shown in Fig. 3(b). The streamwise dimension of the monitored area is $40D$ and the transverse dimension is $30D$. The image resolution of 1280×1024 pixels and the shooting frequency of

5000 Hz were specified. Hollow glass spheres, with a mean diameter of 20 μm and density of 1.05–1.15 g/cm^3 were used as tracing particles. The particles traveled with water. An individual data group was composed of 2000 consecutive images, which were processed to calculate average flow quantities.
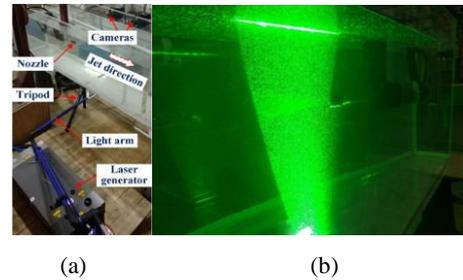

Fig. 3. Setup of flow measurement: (a) configuration of optical components; (b) light emitting scene

The sampling frequency of a conventional PIV system is generally lower than 150 Hz. Since the waterjet pressures adopted in present experiment are rather high, some transiently varying flow structures cannot be captured. The introduction of TR-PIV made up for such a deficiency. For the TR-PIV system used here, the maximum laser power attains 66.6 W and the maximum pulsation energy is 70 mJ. Therefore, the waterjet images can be recorded at small temporal scales; meanwhile, high resolutions can be accomplished to guarantee high accuracy of the post-processing of these images.

3. FLOW CHARACTERISTICS OF THE SUBMERGED WATERJET

Velocity data acquired at waterjet pressures p=5 and 15 MPa were processed and the cross-sectional distributions of average velocity are plotted in Fig.4. For each case, four cross sections along the streamwise direction are selected. Meanwhile, velocity is non-dimensionalized relative to the maximum waterjet velocity for each case. It is noteworthy that the waterjet stream segment corresponding to $0 < x < 5D$ cannot be handled since the segment is highly coherent and thin. Hitherto, such a segment has only been treated at low waterjet pressures (Gong *et al*. 2016).

The similarity between the two cases presented in Fig. 4 is evidenced based on corresponding velocity distributions. Meanwhile, for each case, overall flow velocity attenuates continuously as the waterjet stream progresses downstream, which is ascribed to the high resistance from ambient water. There is a high-velocity spike near the nozzle outlet, which is shared by the two cases. Such a velocity spike contributes significantly to the impact capability of the waterjet stream. In comparison, the length of the core area of the waterjet stream at p=15 MPa is slightly larger than its counterpart. Furthermore, at x=27D, the cross-sectional velocity distribution
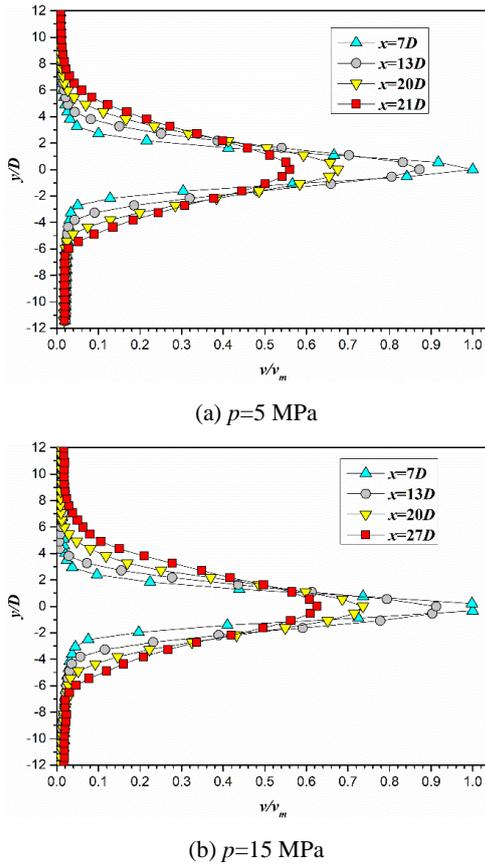
(a) *p*=5 MPa

(b) *p*=15 MPa

Fig. 4. Cross-sectional distributions of average velocity.

exhibits the form of Gaussian distribution, signifying the development of the waterjet has achieved a fully developed state.

4. WATERJET FLOW PATTERNS

4.1 POD Approach

The proper orthogonal decomposition (POD) approach has been used to decompose complex flow field into characteristic modes. With the first few POD modes, large-scale coherent structures can be identified through flow parameter distributions (Tang *et al*. 2015). Meanwhile, the relationship between flow structures and the energy carried by the flow can be established via the POD approach. Essentially, the first few POD modes assume a high percentage of the total jet flow energy (Watanabe *et al.* 2015). From the mathematical aspect, the aim of the POD approach is to seek the optimal orthogonal coordinates. As the flow field is projected onto the optimal orthogonal coordinates, the average energy is greater than that of the flow field projected along any other coordinates.

The number of velocity fields obtained using TR-PIV is expressed by *m*, and each velocity field is represented by a two-dimensional matrix, *V*, which contains $m_1 \times m_2$ elements. The elements in the matrix are represented by v_{mn}. Then the correlation

between different flow fields can be expressed with the covariance matrix A_{ij}:

$$A_{ij} = \frac{1}{m_1 \times m_2} \sum_{m=1}^{m_1} \sum_{n=1}^{m_2} V(v_{mn}, t_i) V(v_{mn}, t_j) \tag{1}$$

where t_i and t_j stand for the moments corresponding to the two instantaneous velocities.

An orthogonal decomposition of A_{ij} yields eigenvalues and corresponding eigenvectors, then each POD mode is obtained with:

$$\varphi^i = \sum_{j=1}^{k} \alpha_j^i V^j \tag{2}$$

where α^i represents eigenvalues and α_j^i is the *j*th element of the eigenvector $\{\alpha^i\}$.

The eigenvalue represents the percentage of the total waterjet energy assumed for each POD mode. In general, the eigenvalue decreases remarkably in the eigenvalue array; therefore, dominant characteristics of the flow are anticipated to be reflected by the first POD modes. Here, the snapshot POD method proposed by Sirovich (1987) was selected. This method employs the temporal correlation matrix instead of the spatial correlation matrix. Therefore, in the presence of a huge amount of velocity data, the calculation procedure will be considerably simplified.
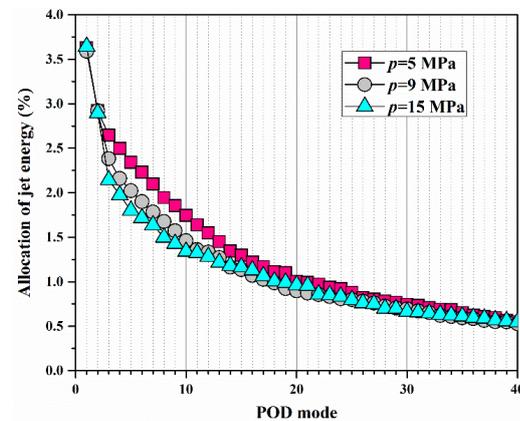

Fig.5. Energy allocation among different POD modes

4.2 Flow Structures at Various POD Modes

At *p*=5, 9 and 15 MPa, the velocity data acquired using TR-PIV were treated using the snapshot POD method. Total waterjet energy was allocated among a spectrum of the POD modes, as indicated in Fig. 5. The three curves are close to each other, particularly at high POD modes. A monotonous decrease in the energy percentage is seen as the order of the POD mode increases, which is shared by the three cases. Furthermore, the energy assumed
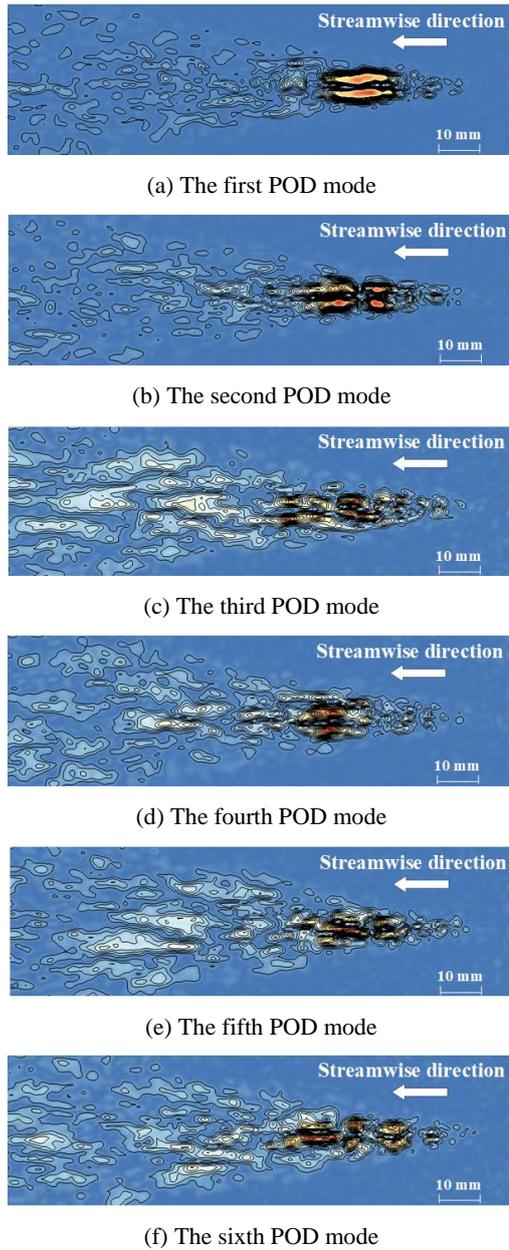
(a) The first POD mode

(a) The first POD mode

(b) The second POD mode

(b) The second POD mode

(c) The third POD mode

(c) The third POD mode

(d) The fourth POD mode

(d) The fourth POD mode

(e) The fifth POD mode

(e) The fifth POD mode

(f) The sixth POD mode

(f) The sixth POD mode

Fig. 6. Flow structures for the first six POD modes at *p*=5 MPa

Fig. 7. Flow structures corresponding to the first six POD modes at *p*=9 MPa

by the first six modes is approximately 17% of the overall waterjet energy, which is common for the three cases. It is inferable that the first six modes determine the main characteristics of the waterjet flows considered.

At *p*=5 MPa, flow structures for the first six POD modes were constructed based on vorticity distributions, as shown in Fig. 6, where the nozzle outlet section is denoted with a red vertical bar. The first mode is featured by two high-vorticity bands which are symmetrically distributed with respect to the nozzle axis. It is noticeable that in streamwise direction, the high-vorticity bands approach the
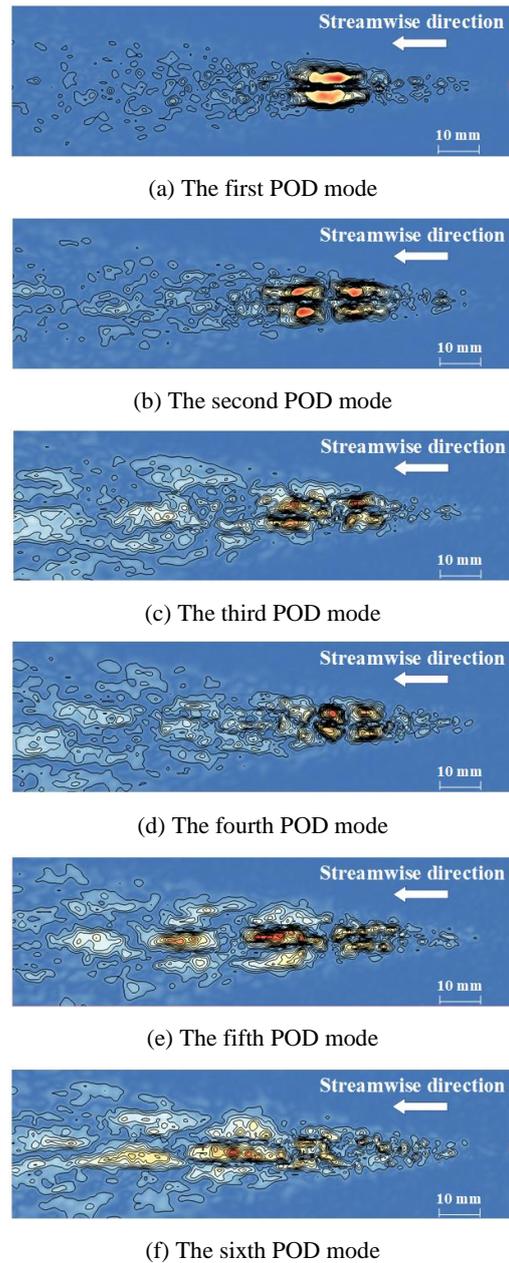
nozzle outlet. This implies that the formation of the flow structures is enabled immediately after the sudden expansion of the waterjet stream as it is issued from the nozzle. For the second mode, each high-vorticity band is divided into two successive shorter bands. The symmetry with respect to the nozzle axis is remained although waterjet energy attenuates. In this case, the characteristics of the flow structures obtained here are to some extent analogous to that of the waterjet issued at low Reynolds number (He and Liu 2017). High vorticity at the edge of the waterjet stream dominates the waterjet flow, which is a distinct feature of the

submerged waterjet and is insensitive to the variation of the waterjet pressure. Meanwhile, the nozzle outlet diameter significantly influences the clearance between the two high-vorticity zones. Since the nozzle diameter is rather small in present experiment, the two high-vorticity bands are nearly connected. For the third mode, the collapse of the high-vorticity bands is apparent; meanwhile, discretely distributed vorticity elements are observed further downstream. The other three modes contain less waterjet energy and the vorticity elements tend to be distributed homogeneously in the waterjet stream with the increase in the order of the POD mode.

In a similar manner, flow structures at *p*=9 MPa are illustrated in Fig. 7. It is seen that the first mode is characterized by two high-vorticity bands downstream of the nozzle, which are similar to those shown in Fig. 6(a). However, the vorticity magnitude increases with the waterjet pressure. As the order of the POD mode increases, the energy concentration decays and large-scale flow structures are replaced with sparsely distributed small-scale flow structures. Moreover, the overall distribution of the flow structures is compatible with the diffusion of the waterjet stream.

At *p*=15 MPa, the flow structures corresponding to the first six POD modes are shown in Fig. 8. For each POD mode, flow structures shown in Figs. 6, 7 and 8 are overall similar. The difference lies in the vorticity magnitude, which increases continuously with the waterjet pressure. Meanwhile, for the first POD mode, streamwise positions of the cores of the high-vorticity bands change slightly with the waterjet pressure but without any certain tendency. As the waterjet pressure increases, velocity gradients between the waterjet stream and ambient water are improved. However, the morphological features of those dominant flow structures remain nearly invariant as the waterjet pressure varies. This manifests an explicit mechanism underlying the formation of the flow structures in the submerged waterjet. Meanwhile, a global view of the first six POD modes indicates that the submerged waterjet is characterized by flow structures of multiple scales. They consume kinetic energy but sustain respectively consistent geometric or kinetic characteristics of the waterjet stream. Provided that cavitation bubbles are produced in the waterjet stream or in adjacent flows, they will inevitably interact with the flow structures. Literally, particular attentions have been devoted to the complex interaction between cavitation bubbles and those distinct flow structures.

5. WATERJET CAVITATION

5.1 Waterjet Cavitation Visualization

Thus far, no relationship has been formulated to correlate the occurrence of cavitation with flow structures of the submerged waterjet. For the submerged waterjet, high waterjet velocity might induce cavitation; meanwhile, the downstream
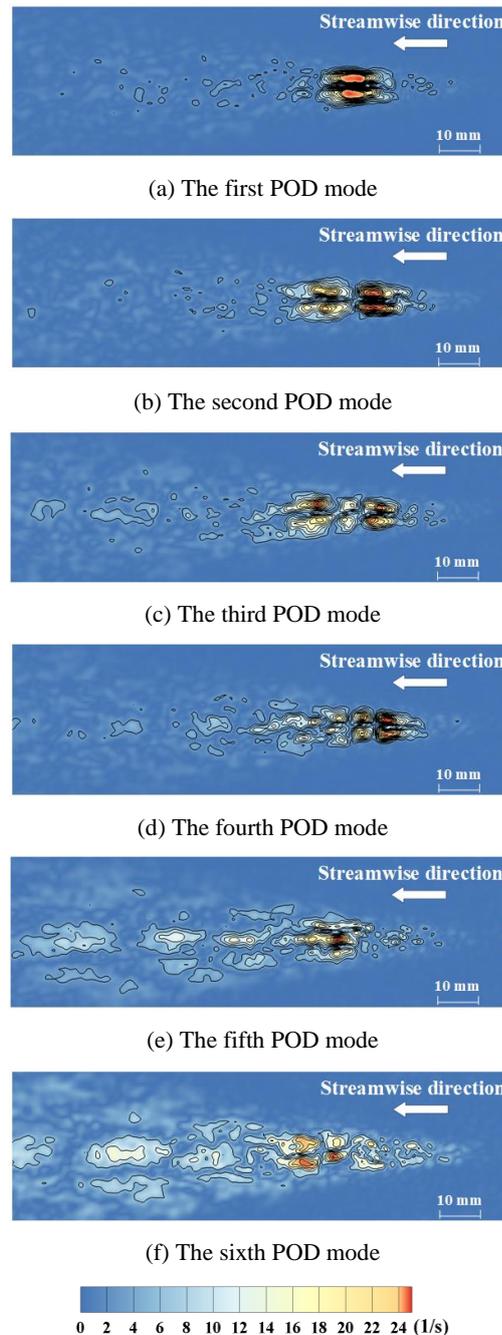

(a) The first POD mode

(b) The second POD mode

(c) The third POD mode

(d) The fourth POD mode

(e) The fifth POD mode

(f) The sixth POD mode

0 2 4 6 8 10 12 14 16 18 20 22 24 (1/s)

Fig. 8. Flow structures corresponding to the first six POD modes at *p*=15 MPa.

pressure, alternatively, the background pressure, can also be tuned to produce cavitation. It is noteworthy that the downstream pressure is a necessary constituent for the definition formula of the cavitation number (Guo *et al.* 2013). Cavitation phenomenon emerging in the submerged waterjet exhibits salient patterns. A typical instantaneous waterjet cavitation image presented in (Wright *et al.* 2013) is shown in Fig. 9. It is clear that dense but non-continuous cavitation clouds develop in streamwise direction. The profiles of the cavitation clouds are rather coarse. In this case, the nozzle is characterized by a flow passage comprising a highly

contracted segment and a straight downstream segment. The upper image is the raw image of cavitation clouds. The image-processing technique enables accurate detection of the profile of the cavitation clouds, resulting to the lower image. Meanwhile, the transverse expansion of the cavitation clouds is not apparent at first; then with the progression of the waterjet stream, an abrupt expansion in transverse direction is illustrated. According to the data presented in (Wright *et al.* 2013), the position where the expansion arises is approximately 16D from the nozzle outlet. Furthermore, the profile of the cavitation zone is related to both nozzle geometry and the waterjet pressure. Moreover, away from the nozzle, the small cavitation clouds have irregular shapes and they shrink apparently further downstream.
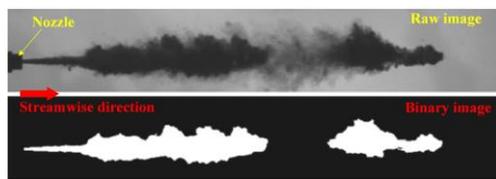

Fig. 9. Typical waterjet cavitation image (Wright *et al*. 2013)

5.2 Cavitation Patterns at Different Waterjet Pressures

In present experiment, as the waterjet pressure is lower than 16 MPa, no cavity is identifiable. As the waterjet pressure increases gradually to p=16 MPa, tiny cavities are observed and the sequential images illustrating the evolution of these cavities are shown in Fig.10, where the nozzle outlet section is marked as a red vertical bar. In the images, tiny black spots denote tracing particles, which were seeded for velocity measurement. At t=t_0, a cavitation bubble cluster is discharged from the nozzle. This features an initial stage of the development of the waterjet cavitation. As the waterjet develops, individual cavities are formed near the nozzle at different moments. At t=t_0+12.2 ms, the integrity of the cavitation zone is impaired and smaller cavities are scattered near the nozzle. Hence, cavity is absent until t=t_0+72.6 ms, at which a small cavity is discernable. At t=t_0+91.8 ms, cavity is close to the nozzle compared to its counterparts shown in Fig.10(a) and (c). Essentially, the images shown in Fig. 10 represent the state of cavitation inception. In this case, the time intervals between neighboring cavity images are rather long and the volume fraction of cavitation is low. Regarding the positions of the cavities, they are apparently in accordance with the positions where the dominant flow structures are extracted via the POD method.

As the waterjet pressure is increased to 17 MPa, consecutive images of cavities are shown in Fig.11. Based on a comparison of the time intervals between Figs. 11 and 10, it is evidenced that the

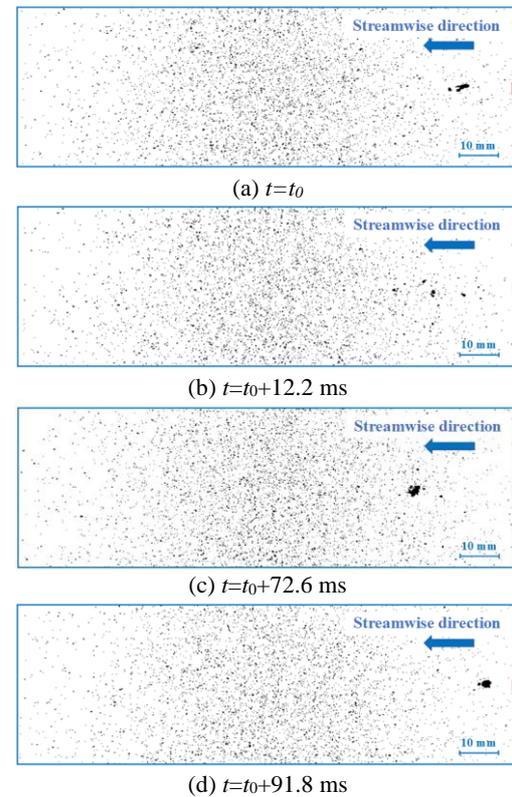frequency of cavitation emergence increases with the waterjet

(a) t=t_0

(b) t=t_0+12.2 ms

(c) t=t_0+72.6 ms

(d) t=t_0+91.8 ms

Fig. 10. Small individual cavities at *p*=16 MPa

pressure. In Fig.11, the development of cavitation apparently undergoes an unstable state, which is symbolized by small cavities that are distributed sparsely in the streamwise direction. Although applying TR-PIV for the velocity measurement under cavitation conditions may yield spurious results, it is deducible that high waterjet pressures lead to intensified interaction between the waterjet stream and ambient water. High vorticity magnitude will be obtained due to high velocity gradients at the edge of the waterjet stream. Furthermore, the cavities approach the nozzle outlet, demonstrating that they can survive under the condition of high waterjet velocity and high vorticity.

Furthermore, in the four subfigures included in Fig.11, the cavity profiles are remarkably different. It is evidenced that large cavities are difficult to form. For the cavities displayed, their trajectories are in accordance with instantaneous waterjet flow patterns. Small cavities can well follow the waterjet flow. A comparison between Figs.10 and 11 indicates that the augment of 1 MPa in the waterjet pressure contributes insignificantly to the increase in the cavitation volume fraction.

At p=19 MPa, four typical cavity images are shown in Fig. 12. It is indicated that the expansion of cavities is considerably improved as compared to those shown in Figs. 10 and 11. Meanwhile, the
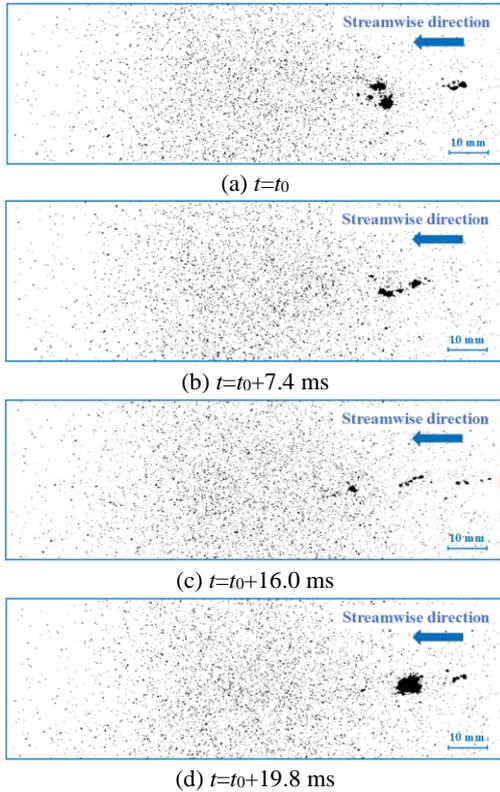
(a) $t=t_0$

(b) $t=t_0+7.4$ ms

(c) $t=t_0+16.0$ ms

(d) $t=t_0+19.8$ ms

Fig. 11. Cavity patterns at $p=17$ MPa

(a) $t=t_0$

(b) $t=t_0+7.8$ ms
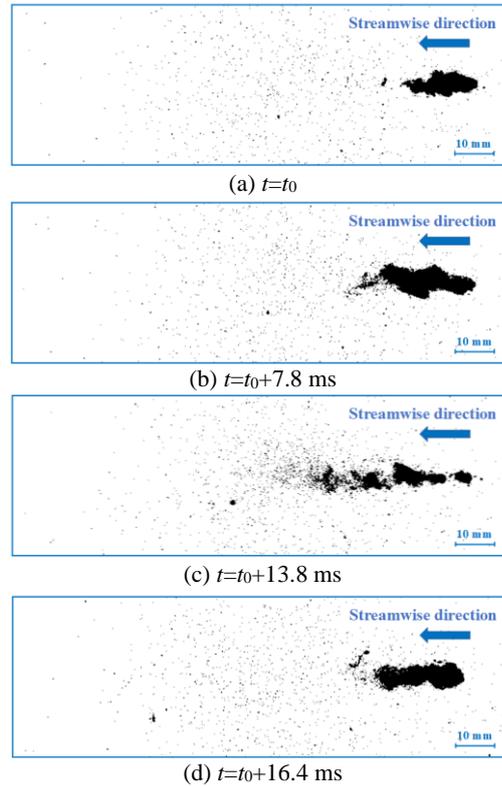

(c) $t=t_0+13.8$ ms

(d) $t=t_0+16.4$ ms

Fig. 12. Cavity patterns at $p=19$ MPa

intermittency of cavitation evolution is clearly manifested from the four subfigures. With reference to the POD results, the positions where cavities gather correspond to the high-vorticity zones. Moreover, the cavitation patterns shown in Fig. 12 are various. Vorticity is related to cavitation, alternatively, high vorticity promotes the occurrence of cavitation. With the development of the waterjet, the integrated high-vorticity zone is replaced with small vorticity elements. In this case, discretely distributed cavities tend to arise further downstream, which reasonable explains the correspondence between cavitation and flow structures. Furthermore, although small vorticity elements assume a rather limited fraction of the total waterjet energy, their contribution to the collapse of large cavities is non-negligible.

Another distinct feature of Fig. 12(c) is that cavities extend or contract remarkably in streamwise direction. The cavities shown in Fig. 12(a), (b) and (d) are concentrated while in Fig. 12(c), lengthened. Therefore, the frequencies of the development of waterjet cavitation cover a wide spectrum.

At a waterjet pressure of 20 MPa, instantaneous cavity patterns are shown in Fig. 13. The cavitation volume fraction does not vary much compared to that indicated in Fig. 12. The most significant difference between Figs.13 and 12 is the overall frequency of cavitation emergence increases with the waterjet pressure. Similarly, the cavitation evolution illustrated in Fig. 13 is not dominated by any single frequency, and a frequency spectrum is anticipated.

A further increase of the waterjet pressure by 1 MPa triggers a significant change of cavitation patterns, as shown in Figs.14 and 13. Stable cavitation clouds are observed; meanwhile, overall cavity length in streamwise direction is increased. Compared to the cavitation image shown in Fig.9, the cavitation clouds obtained here exhibit different patterns; particularly, away from the nozzle, cavitation clouds rapidly diffuse and the coherent cavitation zones cannot sustain any more. More detailed quantitative information of the morphology of the cavities can be obtained using the image-processing methods. In this case, the gray scale method has often been used to treat the captured images (Soyama *et al.* 1996). Hence, the geometric parameters of the cavities can be statistically calculated.

In Fig. 15, the waterjet pressure attains 22 MPa, the overall profiles of the cavitation zone remain similar to those shown in Fig. 14. However, the lateral expansion of the front of the cavitation zone is explicitly improved with increasing waterjet pressure. Meanwhile, the cavitation zone near the nozzle swells in lateral direction. This agrees with the intensified diffusion of the waterjet stream due to the increase in the waterjet pressure.

From another viewpoint, as the waterjet pressure increases, the energy delivered to the waterjet stream is increased. Consequently, the disturbance of the waterjet stream to ambient water is reinforced due to the introduction of cavitation.
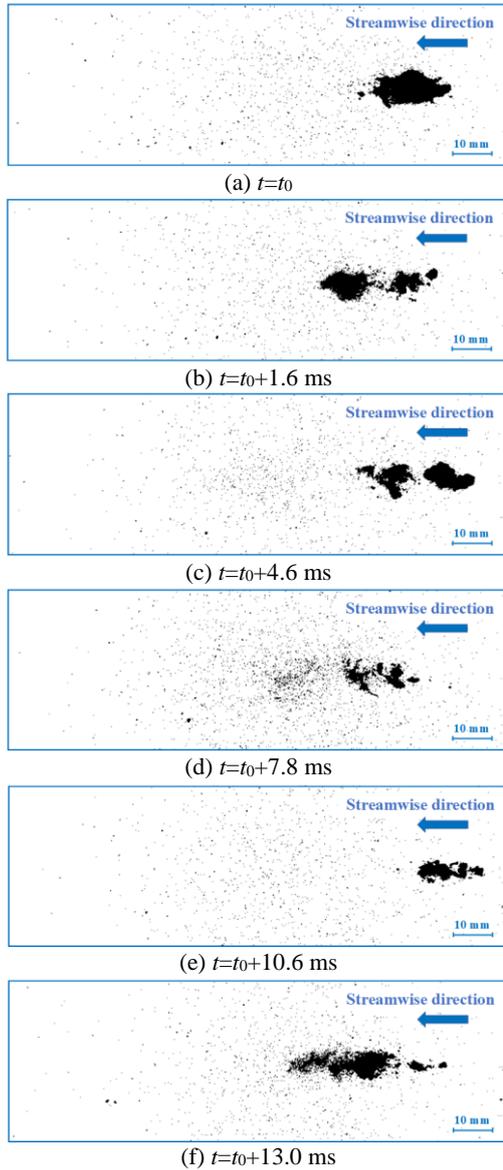
(a) $t=t_0$

(b) $t=t_0+1.6$ ms

(c) $t=t_0+4.6$ ms

(d) $t=t_0+7.8$ ms

(e) $t=t_0+10.6$ ms

(f) $t=t_0+13.0$ ms

Fig. 13. Cavity patterns at $p=20$ MPa

(a) $t=t_0$

(b) $t=t_0+1.0$ ms

(c) $t=t_0+2.4$ ms

(d) $t=t_0+4.6$ ms

Fig. 14. Cavity clouds at $p=21$ MPa

(a) $t=t_0$

(b) $t=t_0+1.0$ ms

(c) $t=t_0+2.2$ ms

(d) $t=t_0+3.2$ ms

Fig. 15. Variation of cavitation clouds at $p=22$ MPa

5.3 Statistical Characteristics of Waterjet Cavitation

The cavitation evolution frequency and the streamwise distance covered by cavities are two quantities that can be used to characterize cavitation (Fortes-Patella *et al.* 2013). Moreover, the two quantities can be used to evaluate the cavitation erosion capability of the waterjet. Based on the images captured using the high-speed camera, a statistical investigation was performed. Each image group was composed of 1600 to 2000 images; the exact number of images depends on the variation frequency of cavities. At different waterjet pressures, the cavitation evolution frequency and the attainable streamwise distance of the cavities are plotted in Fig. 16, where f_{cav} denotes the cavitation evolution frequency and L_{cav} the attainable streamwise distance of cavities. Meanwhile, the variation range of each quantity is indicated in Fig. 16.
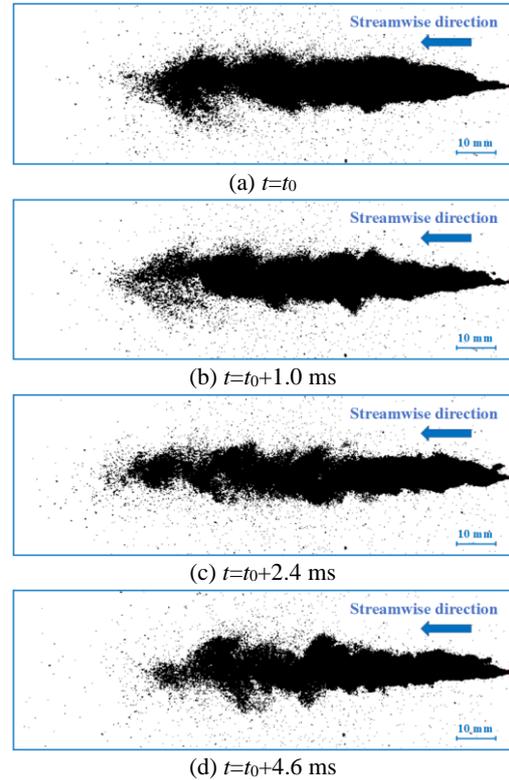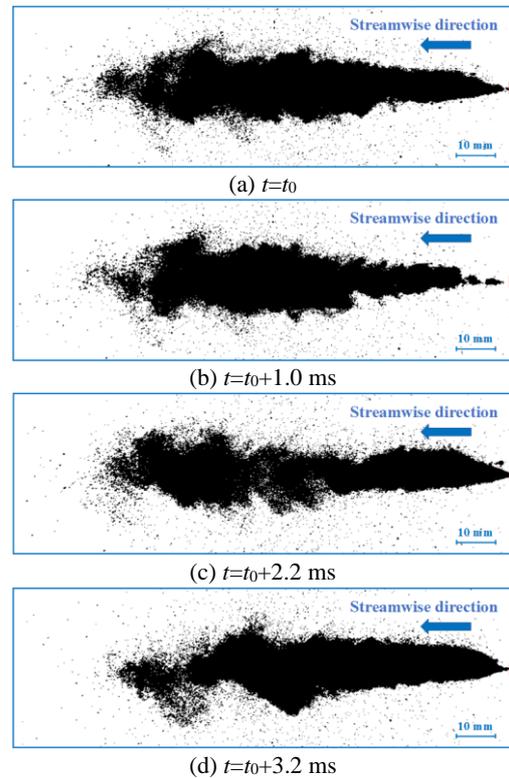
A global view of Fig.16 indicates that the cavitation evolution frequency increases with the waterjet

1265

pressure; however, between the results obtained at p=21 and 22 MPa, the difference in the cavitation evolution frequency is minimized. Meanwhile, the attainable streamwise distance exhibits similar tendencies. Based on the images shown in Fig.11, p=17 MPa corresponds to the situation of cavitation inception. Prior to p=21 MPa, cavitation development is evidently suppressed, which can be judged from Figs.10 to 13. Therefore, such a range of waterjet pressure is associated with the initial stage of cavitation evolution. Meanwhile, extending or shrinking of cavities and the attainable streamwise distance do not abide by any explicit tendency. This is related to the inherent properties of cavitation instead of the image-processing method employed. As the waterjet pressure is higher than 21 MPa, cavitation clouds are relatively stable although the fronts of the cavitation clouds remain oscillating in streamwise direction.
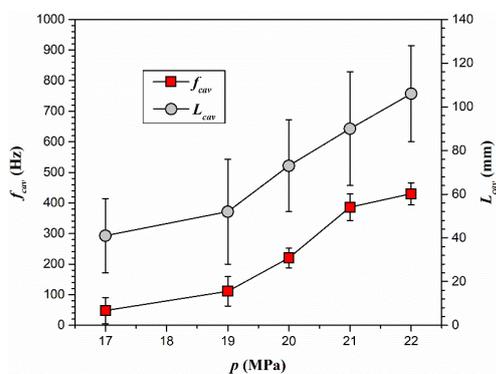

Fig. 16. Cavitation evolution frequency and attainable streamwise distance of cavities

6. CONCLUSIONS

(1) With a nozzle characterized by a short straight segment of flow passage upstream of the nozzle outlet, the similarity of average velocity distributions is remained as the waterjet pressure varies from 5 to 15 MPa. Immediately downstream of the nozzle, velocity difference between the waterjet stream and ambient water is evidenced and is intensified as the waterjet pressure increases.

(2) The first six POD modes assume nearly 17% of the total waterjet energy, as is shared by the three cases with different waterjet pressures. Two closely situated high-vorticity bands represent the most dominant flow structures in the waterjet flow field. As the order of the POD mode increases, large-scale flow structures attenuate and sparsely distributed small-scale flow structures are prevalent.

(3) Cavitation was activated as the waterjet pressure is increased to 16 MPa. Initially, cavitation behaves as single cavities or cavity clusters. Then cavitation bursts evidently. Finally, cavities are merged into cavitation clouds. Both the inception and the development of cavitation are highly relevant to the vorticity distribution. Attainable streamwise

distance increases with the waterjet pressure. Between the cases of p=21 and 22 MPa, the difference of the cavitation evolution frequency is minimized.

REFERENCES

ASTM Standard G134-95. (2010). Standard Test Method for Erosion of Solid Materials by a Cavitating Liquid Jet, ASTM International, West Conshohocken, PA, 2001, www.astm.org

Gong, C., M. Yang, C. Kang and Y. Wang (2016). The acquisition and measurement of surface waves of high-speed liquid jets. *Journal of Visualization* 19(2), 211–224.

Cheng, Y., M. Torregrosa, A. Villegas and F. Diez (2011). Time resolved scanning PIV measurements at fine scales in a turbulent jet. *International Journal of Heat and Fluid Flow* 32(3),708–718.

Fortes-Patella, R., G. Challier and J. Archer (2013). Energy balance in cavitation erosion: from bubble collapse to indentation of material surface. *Journal of Fluids Engineering-Transactions of the ASME* 135(1), 011303.

Giorgi, M., A. Ficarella and M. Tarantino (2013). Evaluating cavitation regimes in an internal orifice at different temperatures using frequency analysis and visualization. *International Journal of Heat and Fluid Flow* 39, 160–172.

Gopalan, S., J. Katz and O. Knio (1999). The flow structure in the near field of jets and its effect on cavitation inception. *Journal of Fluid Mechanics* 398, 1–43.

Guo, S., B. Khoo, S. Teo and H. Lee (2013). The effect of cavitation bubbles on the removal of juvenile barnacles. *Colloids and Surfaces B Biointerfaces* 109, 219–227.

He, C. and Y. Liu (2017). Proper orthogonal decomposition of time-resolved LIF visualization: scalar mixing in a round jet. *Journal of Visualization* 20, 789–815.

Hu, H., Y. Zheng and C. Qin (2010). Comparison of Inconel 625 and Inconel 600 in resistance to cavitation erosion and jet impingement erosion. *Nuclear Engineering and Design* 240(10), 2721–2730.

Kang, C., H. Liu and H. Soyama (2018). Estimation of aggressive intensity of a cavitating jet with

multiple experimental methods, Wear 394-395, 176–186.

Macian, V., R. Payri, X. Margot and F. J. Salvador (2003). A CFD analysis of the influence of diesel nozzle geometry on the inception of cavitation, *Atomization and Sprays* 13, 579–604.

Nobel, A. and A. Talmon (2012). Measurements of the stagnation pressure in the center of a cavitating jet. *Experiments in Fluids* 52(2), 403–415.

Peng, G., A. Wakui, Y. Oguma, S. Shimizu, and H. Ji (2018). Periodic behavior of cavitation cloud shedding in submerged water jets issuing from a sheathed pipe nozzle. *Journal of Flow Control, Measurement & Visualization* 06(1), 15–26.

Petkovšek, M. and M, Dular (2013). Simultaneous observation of cavitation structures and cavitation erosion. *Wear* 300(1-2), 55–64.

Shimada, N., H. Hibara, Y. Ishibashi, M. Sumida and K. Sudo (2004). Analysis of submerged water jets by visualization method: Flow pattern and self-induced vibration of jet. *Journal of Visualization* 7(4), 281–289.

Sirovich, L. (1987). Turbulence and the dynamics of coherent structures: Part I–III. *Quarterly of Applied Mathematics* 45(3), 561–590.

Soyama, H. (2017). Key factors and applications of cavitation peening. *International Journal of Peening Science and Technology* 1, 3–60.

Soyama, H. (2013). Effect of nozzle geometry on a standard cavitation erosion test using a cavitating jet. *Wear* 297, 895–902.

Soyama, H. and F. Takeo (2016). Comparison between cavitation peening and shot peening for extending the fatigue life of a duralumin plate with a hole. *Journal of Materials Processing Technology* 227, 80–87.

Soyama, H., Y. Yanauchi, K. Sato, T. Ikohagi, R. Oba and R. Oshima (1996). High-speed observation of ultrahigh-speed submerged water jets. *Experimental Thermal and Fluid Science* 12(4), 411–416.

Tang, S., L. Djenidi, R. Antonia and Y. Zhou (2015). Comparison between velocity- and vorticity-based POD methods in a turbulent wake. *Experiments in Fluids* 56(8), 1–12.

Watanabe, R., T. Kikuchi, T. Yamagata and N. Fujisawa (2015). Shadowgraph imaging of cavitating jet. *Journal of Flow Control, Measurement & Visualization* 03(3), 106–110.

Wilms, J., T. Beck, C. Sorensen, M. Hosni, S. Eckels and D. Tomasi (2014, November). Experimental measurements and flow visualization of water cavitation through a nozzle. In *Proceedings of the ASME 2014 International Mechanical Engineering Congress and Exposition*, Quebec, Canada.

Wright, M., B. Epps, A. Dropkin and T. Truscott (2013). Cavitation of a submerged jet. *Experiments in Fluids* 54(6), 1541.